


A NUMERICAL 3D FLUID-STRUCTURE INTERACTION MODEL FOR BLOOD FLOW IN A MRI-BASED ATHEROSCLEROTIC ARTERY

NADER EL KHATIB¹, OUALID KAFI² ^{*}, DIANA OLIVEIRA³,
ADÉLIA SEQUEIRA^{2,4} AND JORGE TIAGO^{2,4}

Abstract. Atherosclerosis, as a result of an inflammatory process, is the thickening and loss of elasticity of the walls of arteries that is associated with the formation of atherosclerotic plaques within the arterial intima, which present a double threat. A piece of vulnerable plaque can break off and be carried by the bloodstream until it gets stuck; and plaque that narrows an artery may lead to a thrombus that sticks to the blood vessel's inner wall. The purpose of the present article is to compare effects across different atheromatous plaque material assumptions on hemodynamics and biomechanics within a partly patient-specific computational domain representing an atherosclerotic artery. A full scale 3D FSI numerical model is implemented and different material hyperelastic assumptions are considered for comparison purposes. The 3D realistic geometry is reconstructed from a medical image. This technique may be useful, specially with the recent advances in computer-aided design (CAD), medical imaging, and 3D printing technologies that have provided a rapid and cost efficient method to generate arterial stenotic biomodels, making in vitro studies a valuable and powerful tool. To understand our results, hemodynamic parameters and structural stress analysis were performed. The results are consistent with previous findings.

Mathematics Subject Classification. 58F15; 58F17; 53C35

Received August 25, 2022. Accepted March 9, 2023.

1. INTRODUCTION

Carotids are arteries supplying blood to the brain, neck and face. Carotid atherosclerosis is the main pathology to fear. Relatively common with age, it could lead to a stroke. The common carotid artery (CCA) arises from the aorta and ascends in the neck. It divides at the level of the middle part of the neck into two arteries: the internal carotid artery (ICA) and the external carotid artery (ECA). This junction zone is called carotid bifurcation. Carotid artery stenoses occur, in most of the cases, at this bifurcation as a consequence of atherosclerosis. Thus, any risk factor predisposing a patient to progressive atherosclerosis can potentially manifest itself as stenosis of the carotid artery with resultant ischemic stroke and (or) transient ischemic attack-like symptoms [39]. Hence,

Keywords and phrases: Atherosclerosis, blood flow, fluid-structure interaction, MRI imaging.

¹ Department of CS and Math., Lebanese American University, Byblos, Lebanon.

² CEMAT – Center for Computational and Stochastic Mathematics, Univ. Lisboa, Lisbon, Portugal.

³ Department of Mechanical Engineering, University College London, London, UK.

⁴ Department of Mathematics, Instituto Superior Técnico, Univ. Lisboa, Lisbon, Portugal.

* Corresponding author: oualid.kafi@tecnico.ulisboa.pt

diagnosis, prevention, and treatment of the carotid atherosclerosis play a pivotal role in stroke prevention, although the notion that atherosclerosis can be prevented or mitigated by vaccination is now moving towards clinical trials [20], since the rate of the asymptomatic chronic occlusion is higher than the symptomatic one.

Hemodynamic and vascular properties have a profound impact on the initiation, progression and rupture of the stenosis in the carotid region [32]. Mechanical effects such as wall shear stress (WSS), pressure forces and structural stress are the most important factors. It is well accepted that low WSS is associated with the formation of plaques, whereas high WSS may impose higher risk of plaque rupture. Also, structural stresses are known to significantly affect the plaque vulnerability due to its considerable contribution to the total mechanical load [7]. Therefore, WSS and structural stress play important roles in view of risk evolution of plaque rupture.

Several computational fluid dynamics (CFD) approaches have been proposed for modeling blood flow. These can be based on idealized geometries, but also on patient-specific geometries taken from medical imaging modalities, such as magnetic resonance imaging (MRI). When using CFD, it is also possible to consider specific viscosity models and investigate the differences in WSS-based descriptors and pressure gradient. In particular, Newtonian and non-Newtonian models have been considered for the case of carotid arteries, both from patients with different carotid stenosis and healthy volunteers [30]. Furthermore, coupling such CFD models with structural ones gives a powerful tool to understand further details in the blood fluid dynamics since the arterial wall also deforms with the action of blood. A suitable fluid-structure interaction (FSI) numerical method is the so-called Arbitrary Lagrangian Eulerian (ALE) formulation. ALE allows points in the vessel structure at every time step, as well as the points inside the fluid domain, to track the displacement. It is the most widely used technique and has been shown to provide accurate numerical simulations [12, 23, 34]. These models can, therefore, be used to assess how different plaque material property assumptions affect computational predictions in an atherosclerotic artery. Computed WSS and structural stresses on such an artery are greatly dependent on material property implementations for the arterial wall and the plaque itself. Such a numerical platform is, therefore, useful to non-invasively determine the biomechanics and hemodynamics associated with different material assumptions. See [9, 19, 25] and the references therein.

Our main goal is to present a noninvasive approach to quantify several hemodynamic parameters and structural stress at the human carotid bifurcation with different material assumptions in the stenosed artery. The approach is based on a combination of MRI and FSI modeling. In a previous study [14], we proposed a 3D FSI model incorporating fluid-structure interaction (blood-plaque and blood-wall) and shear-thinning hemodynamics effects in a 3D idealized geometry were considered. Flow and structures stresses were analyzed.

In the present work we adopt a patient-specific imaged-based strategy. Based on the geometric techniques recently used in [35] in the frame of aortopathies, we reconstruct both the atherosclerotic plaque and the remaining healthier artery wall. We present and study a model of blood-plaque and blood-wall interaction in the realistic case of a three-dimensional geometry, where the computing domain is a stenosed carotid bifurcation resulting from medical imaging. We will then analyze several computational indices under the light of previous results such as those in [4, 14, 35], which will be potentially useful for future studies considering atherosclerosis, especially concerning the choice of material properties.

2. METHODS

2.1. 3D geometry construction

Our image-based modeling approach involves the following steps. First, the lumen geometry of the stenotic carotid artery that will be used in our simulations is derived from MRI (see Fig. 1a). Then the plaque and the wall structures are artificially added. To construct such geometry, several free computational tools are available, such as ITK-SNAP, SimVascular or 3DSlicer. Also commercial options such as Simpleware Scan IP, may be used. This geometry consists of the lumen, that is the interior of the artery. Moreover, the branches were extended (see Fig. 1b) to avoid abnormal entrance (inlet) and exit (outlet) effects that may occur due to the artificial truncation of the domain. Indeed, the inlet extension allows the flow to be fully developed when entering the domain of interest, and the outlet extensions avoid spurious pressure wave reflections.

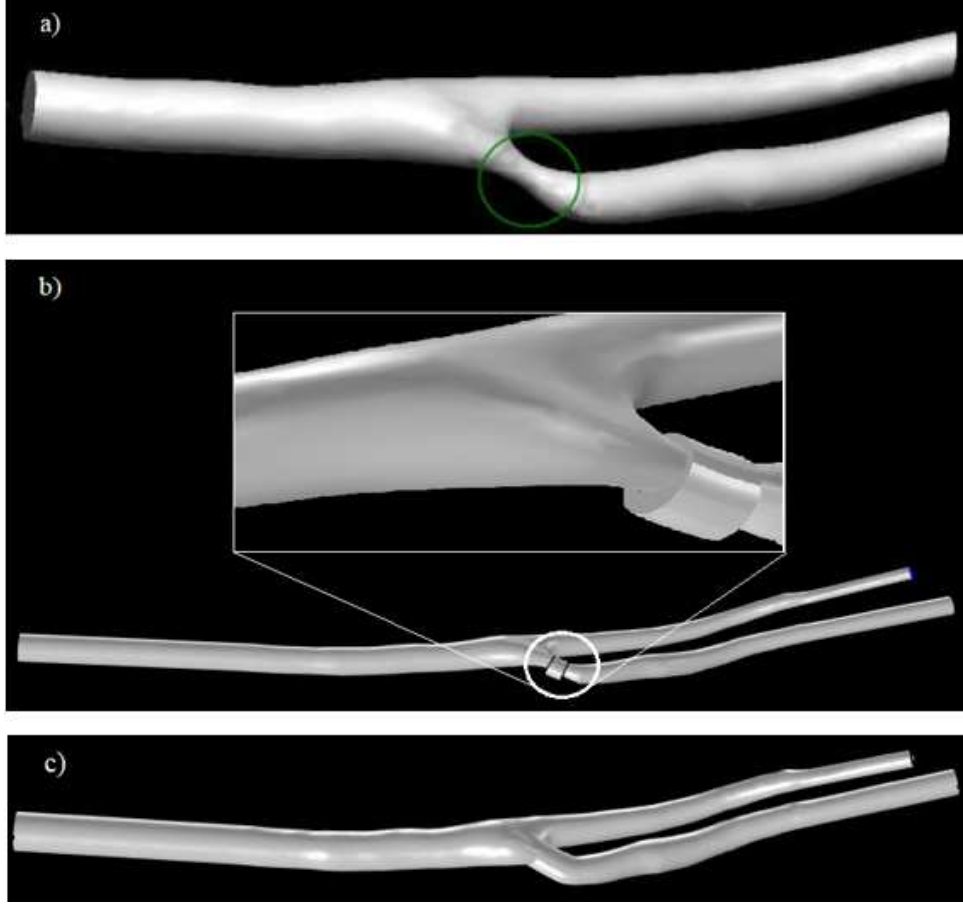


FIGURE 1. a) Medical image of the lumen of a carotid bifurcation with a stenotic region [13]. b) The extended lumen with the plaque construction. c) Computational domain after fibrous cap, lipid pool and vascular wall construction.

Finally, the last realistic geometry was obtained in MeshLab in order to repair and smooth the model surface. Then, in order to design the FSI model, an open-source tool obtained from the finite element library LifeV developed in Politecnico di Milano [15] was used to generate the wall from the vessel lumen surface model previously obtained (see Fig. 1c).

After wall model surface discretization in Mesh-Lab and file type conversion in SolidWorks 2010, the model was imported into COMSOL Multiphysics for numerical FSI modeling and simulations.

2.2. FSI modeling

2.2.1. Fluid model

As we are dealing with arteries with sufficiently large diameters, here we consider blood as an incompressible fluid, described by the quasi-Newtonian equations for the conservation of mass and linear momentum, as follows:

$$\begin{aligned} \rho_f \frac{\partial \mathbf{u}}{\partial t} + \rho_f (\mathbf{u} \cdot \nabla) \mathbf{u} - \nabla \cdot (2\mu(\mathbf{s}(\mathbf{u})) \mathbf{D}\mathbf{u}) + \nabla p &= 0 \\ \nabla \cdot \mathbf{u} &= 0. \end{aligned} \quad (2.1)$$

This system of time dependent partial differential equations involves the blood velocity $\mathbf{u} = [\mathbf{u}_1, \mathbf{u}_2, \mathbf{u}_3]^T$ and the pressure p as the unknown variables. The dynamic viscosity μ is a function of the strain rate tensor $\mathbf{D}\mathbf{u} = \frac{1}{2}(\nabla\mathbf{u} + (\nabla\mathbf{u})^T)$. More precisely, μ is a function of $\mathbf{s}(\mathbf{u})$, the second invariant of the strain rate tensor, defined by:

$$(\mathbf{s}(\mathbf{u}))^2 = 2\mathbf{D}\mathbf{u} : \mathbf{D}\mathbf{u} = 2 \sum_{i,j} (\mathbf{D}\mathbf{u})_{ij} (\mathbf{D}\mathbf{u})_{ji}.$$

We consider μ defined by the Carreau-Yasuda law,

$$\mu(\mathbf{s}(\mathbf{u})) = \mu_\infty + (\mu_0 - \mu_\infty)(1 + (\lambda\mathbf{s}(\mathbf{u}))^2)^{(n-1)/2},$$

with $\mu_0 = 0.0456$ Pa s (the viscosity at the lowest shear rate), and $\mu_\infty = 0.0032$ Pa s (the viscosity at the highest shear rate), $\lambda = 10.03$ s, $\rho_f = 1060$ kg m $^{-3}$ (the fluid density) and $n = 0.344$ (corresponding to a shear-thinning viscosity fluid). The values of these parameters are taken from [16]. Although for large and almost cylindrical vessels a constant viscosity may be considered, it has been shown that, for stenotic cases, the shear-thinning nature of blood should not be neglected, if one is interested in hemodynamic factors such as recirculation size and WSS magnitudes. See, for instance [19].

2.2.2. Models for artery wall and plaque structures

We are now going to specify the details of the three structural models used in this work. Consider the 3D nonlinear model of hyperelasticity [8], governed by the equation

$$\rho_s \frac{\partial^2 \boldsymbol{\eta}}{\partial t^2} - \mathbf{div}(\mathbf{F}\mathbf{S}) = 0, \tag{2.2}$$

where $\boldsymbol{\eta}$ represents the displacement vector, \mathbf{F} is the deformation gradient tensor, given by $\mathbf{F} = \mathbf{I}_3 + \nabla\boldsymbol{\eta}$ (\mathbf{I}_3 is the identity matrix), and \mathbf{S} represents the second Piola-Kirchhoff stress tensor. \mathbf{S} can be computed as $\mathbf{S} = \frac{\partial\omega}{\partial\boldsymbol{\varepsilon}}$ where the strain tensor $\boldsymbol{\varepsilon}$ is defined by the

$$\boldsymbol{\varepsilon} = \frac{1}{2}(\nabla\boldsymbol{\eta} + (\nabla\boldsymbol{\eta})^T + (\nabla\boldsymbol{\eta})^T \nabla\boldsymbol{\eta}),$$

and ω is the elastic strain energy density, which is material dependent.

In this work we assume the vessel wall to be modeled as a St Venant-Kirchhoff material. Under this assumption, \mathbf{S} becomes defined by the stress-strain relationship

$$\mathbf{S} - \mathbf{S}_0 = \mathbf{C} : (\boldsymbol{\varepsilon} - \boldsymbol{\varepsilon}_0 - \boldsymbol{\varepsilon}_{inel}),$$

where \mathbf{S}_0 and $\boldsymbol{\varepsilon}_0$ represent the initial second Piola-Kirchhoff stress and strain tensors, respectively, $\boldsymbol{\varepsilon}_{inel}$ the inelastic strain tensor and \mathbf{C} the fourth-order stiffness tensor. The symbol “:” stands for the inner product of two second-order tensors. Here, we neglect the effects of \mathbf{S}_0 , $\boldsymbol{\varepsilon}_0$ and $\boldsymbol{\varepsilon}_{inel}$.

The vessel wall is considered isotropic in such a way that the stiffness tensor has no preferred direction and the corresponding tensor components are computed internally according to:

$$\mathbf{C}^{ijkl} = \lambda_s \mathbf{g}^{ij} \mathbf{g}^{kl} + \mu_s (\mathbf{g}^{ik} \mathbf{g}^{jl} + \mathbf{g}^{il} \mathbf{g}^{jk}),$$

TABLE 1. Parameters for the structure's material.

Model structure	Assumption	Parameters
MR-H Fib. Cap	Mooney-Rivlin	$C_{10} = 9200 \text{ N m}^{-2}$, $C_{01} = 0 \text{ N m}^{-2}$, $\kappa = 3000 \text{ MPa}$, density = 1000 kg m^{-3}
MR-H Lip. Pool	Mooney-Rivlin	$C_{10} = 500 \text{ N m}^{-2}$, $C_{01} = 0 \text{ N m}^{-2}$, $\kappa = 200 \text{ MPa}$, Density = 1000 kg m^{-3}
MR-H External Wall	St Venant-Kirchhoff	$\nu = 0.45$, $E = 2 \times 10^6 \text{ Pa}$
NL-H Fib. Cap, L. Pool and Ext. Wall	St Venant-Kirchhoff	$\nu = 0.45$, $E = 2 \times 10^6 \text{ Pa}$
Calcified-M Fib. and L. Pool	St Venant-Kirchhoff	$\nu = 0.45$, $E = 5 \times 10^6 \text{ Pa}$
Calcified-M External Wall	St Venant-Kirchhoff	$\nu = 0.45$, $E = 2 \times 10^6 \text{ Pa}$

where $\lambda_s = \frac{\nu E}{(1-2\nu)(1+\nu)}$ and $\mu_s = \frac{E}{2(1+\nu)}$ are the Lamé coefficients, E is the Young modulus ($E = 2 \cdot 10^6$ Pa), ν is the Poisson ratio ($\nu = 0.45$) and \mathbf{g} the metric tensor. As a result, we could also express the stress in terms of the strain as $\mathbf{S} = \lambda_s \text{tr}(\boldsymbol{\varepsilon})\mathbf{I}_3 + 2\mu_s \boldsymbol{\varepsilon}$.

Concerning the structural domain representing the atheromatous plaque, we are going to consider three different model assumptions. In the first one, we use the same material assumption for the plaque as for the wall. The corresponding full model will be called the Nonlinear Hyperelastic Model (NL-H). Secondly, we assume the plaque to be calcified and, accordingly with [6, 46] we consider an increased value for the Young modulus of $E = 5 \cdot 10^6$ Pa. We will refer to this as the calcified model. The two models resulting from these assumptions, are to a certain extent, classical, and we consider them for comparison purposes. The third model, recently suggested but not yet applied to patient-specific domains, assumes the plaque to behave differently from the wall, specifically, to verify the so-called Mooney-Rivlin Hyperelastic assumption. According to this assumption the second Piola-Kirchhoff stress tensor is given by $\mathbf{S} = \frac{\partial \omega}{\partial \boldsymbol{\varepsilon}}$ with

$$\omega = C_{10}(\bar{I}_1 - 3) + C_{01}(\bar{I}_2 - 3) + \frac{1}{2}\kappa(\bar{J} - 1)^2. \quad (2.3)$$

In (2.3), \bar{J} represents the ratio between the current and original volumes and \bar{I}_1 , \bar{I}_2 are the first two modified strain invariants, to be independent of the volume change ($\bar{I}_1 = I_1/\bar{J}^{2/3}$ and $\bar{I}_2 = I_2/\bar{J}^{4/3}$, where I_1 and I_2 are the first two strain invariants). The use of these modified invariants and the last term in equation (2.3) allows the description of nearly incompressible materials.

We distinguish between the lipid pool and the fibrous cap by choosing the energy function parameter C_{10} , C_{01} and κ in agreement with experimental measurements taken from [28, 42]. We refer to the whole model as (MR-H). In Table 1, we summarize the main features, at the structure level, of the three models.

2.2.3. Coupling and boundary conditions

To couple fluid and structures equations (2.1) and (2.2) we used an ALE formulation. We rewrite the equations of the fluid, the generalized Navier-Stokes equations, in the ALE formulation as

$$\rho_f \frac{\partial \mathbf{u}}{\partial t} \Big|_X + \rho_f ((\mathbf{u} - \mathbf{w}) \cdot \nabla) \mathbf{u} - \nabla_x \cdot (2\mu(\mathbf{s}(\mathbf{u})) \mathbf{D}\mathbf{u}) + \nabla_x p = 0 \quad (2.4)$$

where X is the Lagrangian coordinate and x is the Eulerian coordinate. \mathbf{w} is the domain velocity. If \mathbf{w} is zero, the method is simply an Eulerian approach, otherwise, if \mathbf{w} is equal to the velocity of the fluid then the approach is Lagrangian. \mathbf{w} can vary arbitrarily and continuously from one value to another in the fluid field. Two coupling conditions were also considered at the blood-wall interface,

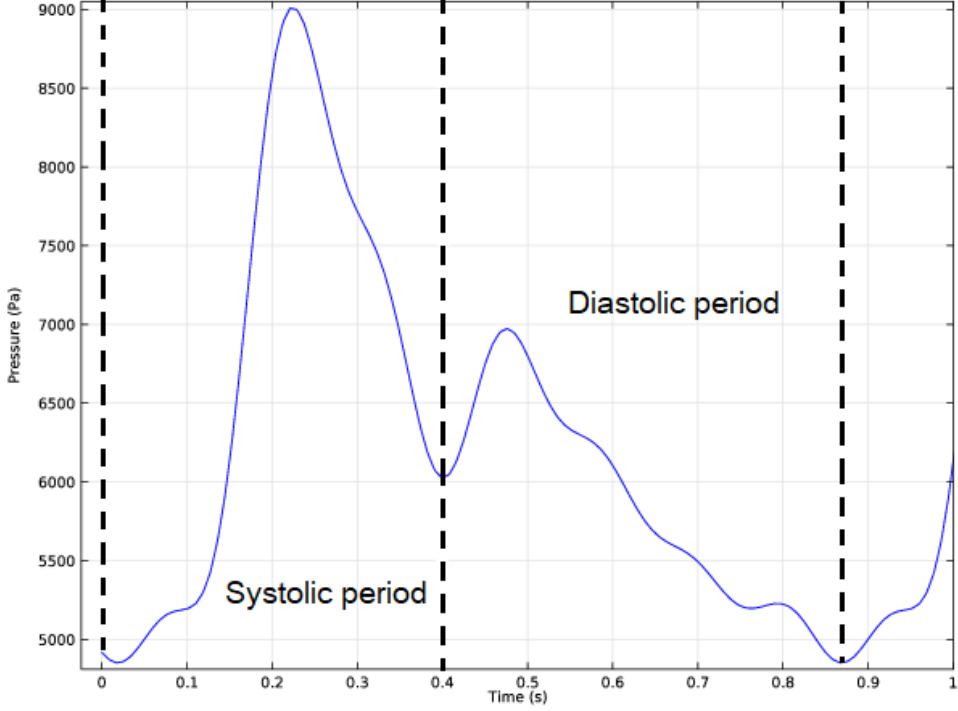


FIGURE 2. Inlet pressure waveform.

- the continuity of the velocity in time

$$\mathbf{u} = \frac{\partial \boldsymbol{\eta}}{\partial t},$$

- and the equilibrium of the stresses

$$-(2\mu(\mathbf{s}(\mathbf{u}))\mathbf{D}\mathbf{u} - p\mathbf{I}_3)\mathbf{n} = J^{-1}\mathbf{F}\mathbf{S}\mathbf{F}\mathbf{n}$$

where $J = \det(\mathbf{F})$ and \mathbf{n} is the outward unit vector to the solid domain

$$-J(2\mu(\mathbf{s}(\mathbf{u}))\mathbf{D}\mathbf{u} - p\mathbf{I}_3)\mathbf{F}^{-T}\mathbf{n}_0 = \mathbf{F}\mathbf{S}\mathbf{n}_0,$$

where \mathbf{n}_0 the outward unit vector to the interface at $t = 0$ (see [24]). The pressure waveform at the inlet is shown in Figure 2. In the following section, the simulations were performed over one cardiac cycle: 0.875 s (systolic and diastolic period).

At the outlets, we consider typical natural BCs where we fix the stress

$$2\mu(\mathbf{s}(\mathbf{u}))\mathbf{D}\mathbf{u} \cdot \mathbf{n} - p\mathbf{n} = -\bar{p}\mathbf{n}. \quad (2.5)$$

$\bar{p} = \frac{\sqrt{\rho_f \beta}}{\sqrt{2}A_0^{5/4}}Q$, where Q is the flow rate and A_0 the cross-section reference area at rest. The coefficient β is related to the mechanical properties of the vessel wall through the expression $\beta = \frac{\sqrt{\pi}h_0E}{1-\nu^2}$, where E is the

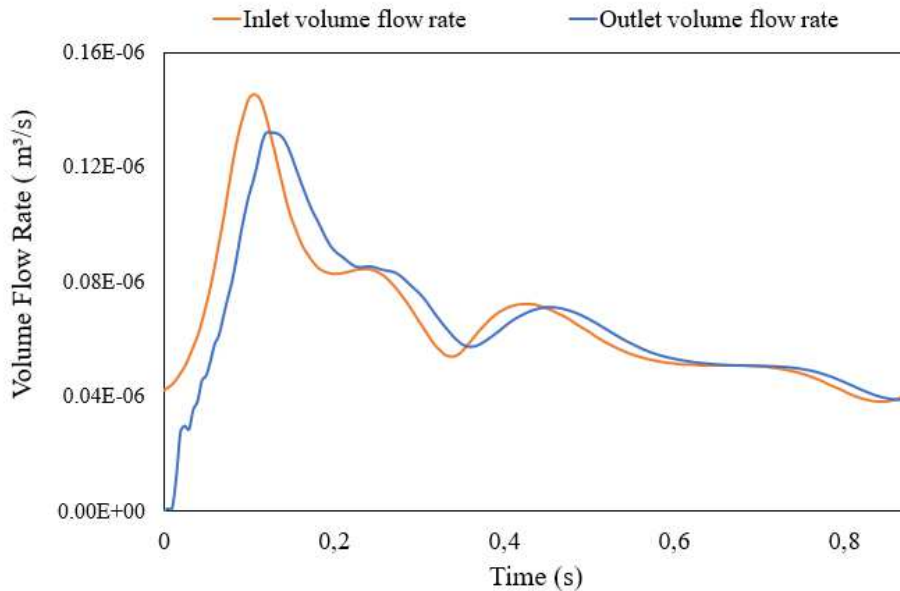


FIGURE 3. Volume flow rate in the inlet and the outlets.

Young modulus, h_0 is the wall thickness and ν is the Poisson ratio. This linear absorbing condition (LAC) has a form of pressure, used in [25] and [40] to reduce significantly the spurious oscillations due to backflow from the outlets in a truncated geometrical domain.

2.3. Computational approach

The resulting coupled system of motion and fluid equations was solved using a finite element space discretization based on P1–P1 stabilized elements for the fluid, and P2 elements for the structure. To overcome the fact that the discrete inf-sup condition is not satisfied when using the same degree finite element for both velocity and pressure, a Galerkin Least Square stabilization [21] was added to the discretization of equation (2.1). This stabilization technique also allows for reducing numerical instabilities due to dominant convective effects resulting from increasing Reynolds numbers. This implies the correct choice of penalization parameters (see [2] and [41]) for equation (2.1), and [5], for equation (2.2).

The time discretization of the fully coupled nonlinear system was done using a backward differentiation formula (IDA solver) with error controlled variable order and adaptive step-size, as described in [22]. The order was allowed to change between 1 and 2. The step size was constrained to a maximum of 5×10^{-3} s. At each time step, the resulting nonlinear system was solved using the Newton–Raphson method [11]. For each linear system, the PARDISO upgrade of the direct solver LEVEL-3 BLAS [37]. For the LU factorization, the matrix reordering algorithm relied on the Nested Dissection Multithreaded [38]. The deformation of the fluid mesh was computed using the so-called hyperelastic smoothing, that is, by minimizing the hyperelastic energy associated to a Neo-Hookean material.

As for the outflow boundary conditions, at each time step the pressure \bar{p} in equation (2.5) is computed explicitly from $Q(t)$ evaluated at the previous time step as

$$\bar{p}(t+1) = \frac{\sqrt{\rho_f \beta}}{\sqrt{2}A_0^{5/4}} Q(t). \quad (2.6)$$

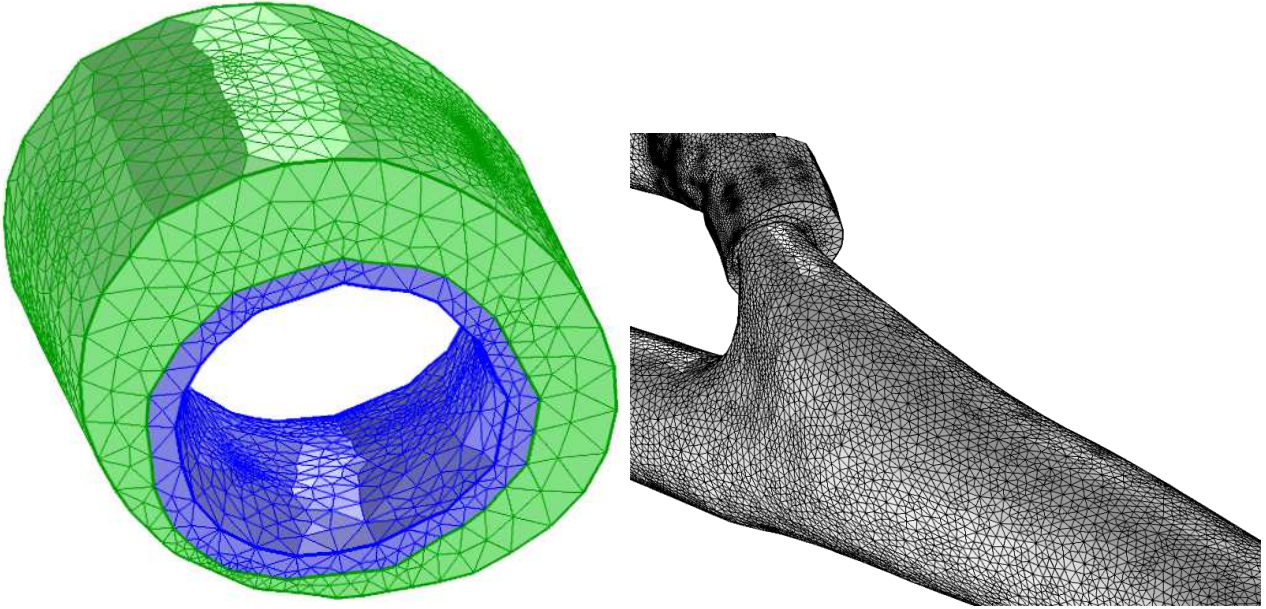


FIGURE 4. Left: the 3D mesh for the lipid pool (green) and the fibrous cap (blue). Right: the 3D mesh for the constructed plaque and the lumen.

TABLE 2. Comparison of the (a) velocity magnitude (m/s), and (b) pressure (Pa) values, obtained within the lumen volume, for different meshes proposed earlier (coarse, intermediate and fine) at different time (s) steps.

	Time (s)	Mesh		
		Coarse	Intermediate	Fine
(a)	0.02	0.13039	0.13076	0.13084
	0.12	0.44505	0.44595	0.44725
	0.22	0.29109	0.29175	0.29102
	0.4	0.23193	0.23342	0.23374
	0.47	0.2418	0.24224	0.24196
	0.875	0.14336	0.14245	0.14315

	Time (s)	Mesh		
		Coarse	Intermediate	Fine
(b)	0.02	2614.6	2606.9	2609
	0.12	13606	13556	13532
	0.22	8621.3	8605.4	8572.8
	0.4	6453.8	6444.1	6429.3
	0.47	6942.4	6930.7	6912.4
	0.875	3818.6	3817	3805.1

Figure 3 presents the volumetric flow rate waveforms in the three arteries, namely at the inlet and outlet boundaries. We can assess the effectiveness of the outlet absorbing boundary conditions (6), by confirming that the flow division between the two daughter arteries is physiologically reasonable.

The simulations were made using Comsol Multiphysics 5.0 in a workstation with a processor Dual CPU Xeon CPU E5-2630 v3 @ 2.4GHz and 128 GB RAM memory was used. In order to improve the accuracy while minimizing the computational cost, we set different element sizes for the mesh approximating the 3D geometry. Therefore, we used smaller element sizes for the lipid pool and the fibrous cap, which are regions characterized by strong gradients and high stresses (see Fig. 4).

All the computations and results presented in the next section were performed with the mesh that corresponds to a total number of degrees of freedom (DOF) of 3 826 996. Additional simulations using a coarse (2 668 968 DOFs) and an intermediate size (3 083 465 DOFs) mesh have been performed to analyze the convergence of the numerical solutions. Figure 5 presents the time-dependent curves obtained under different mesh densities, while Table 2 presents velocity magnitude and pressure values at specific time instants.

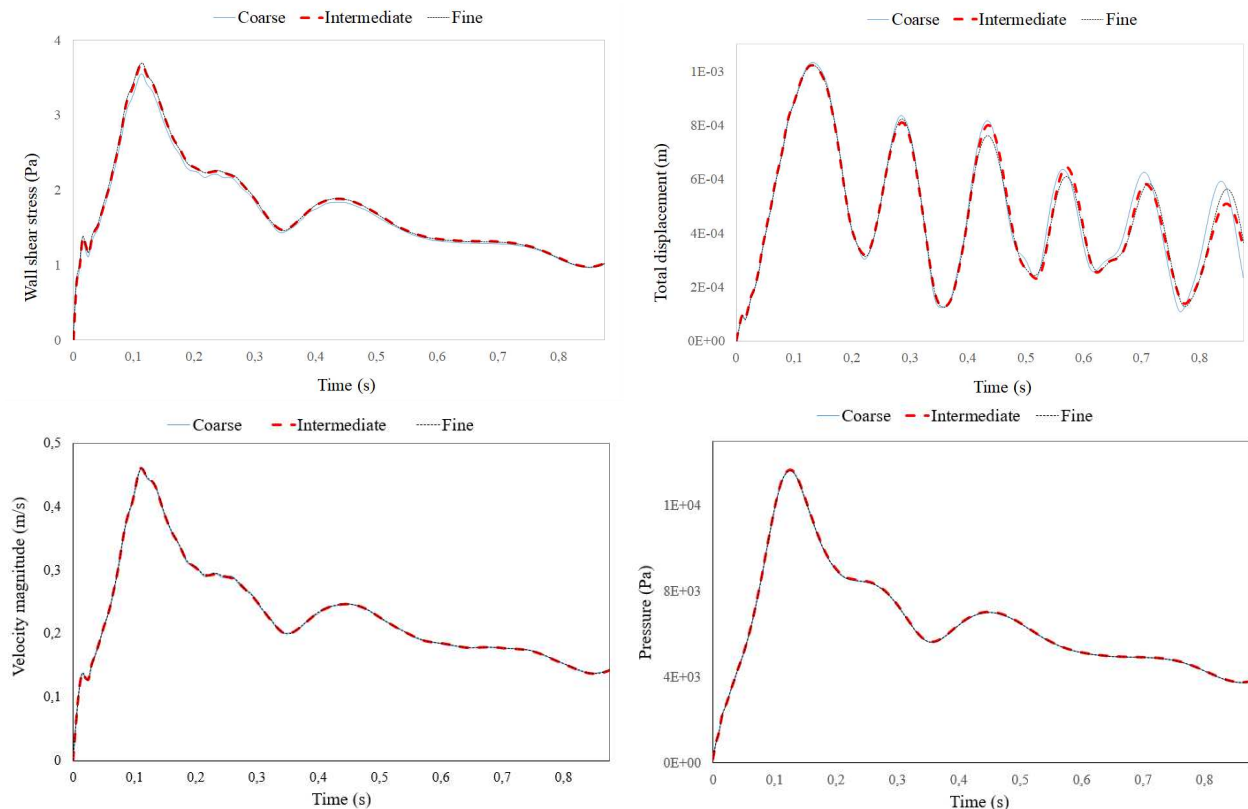


FIGURE 5. First row: comparison between the average values of WSS (left) and the total displacement (right), Second row: comparison between the fluid velocity magnitude (left) and the pressure (right) in a coarse, intermediate size and finer mesh.

In fact, Figure 5 shows that the average values of WSS and the total displacement curves, in the three meshes, follow each other closely. These results show that the difference in functional metrics obtained with the selected mesh (fine) and other assessed meshes is minimum, further showcasing the validity of the use of the mesh with 3 826 996 DOFs for subsequent numerical simulations.

3. RESULTS AND DISCUSSION

In this section, we present and discuss the numerical results obtained for the three models (MR-H, NL-H and calcified model) as described above. In Figures 6–8, we can see velocity patterns, fluid stresses, and structural stresses at three different moments of the cardiac cycle. In Figures 6–8, the position of the plaque at $t = 0$, was depicted using black circular edges. This allows a simultaneous perception of the stenotic branch displacement, at each of the three time instants. Figures 9 and 10 present space averages along the cardiac cycle.

3.1. Flow velocity

Based on the properties of each model mentioned above, the following results allow the analysis of the characteristics of the pulsatile blood flow. Velocity streamlines are depicted in Figure 6 for the MR-H, NL-H and calcified model (the first, second and third row, respectively). Concerning velocity magnitudes, one can observe that the calcified model produces the highest velocities along the cardiac cycle, and that these are located near the stenosis. In the remaining models, the maximum velocities are smaller, and spread further away from

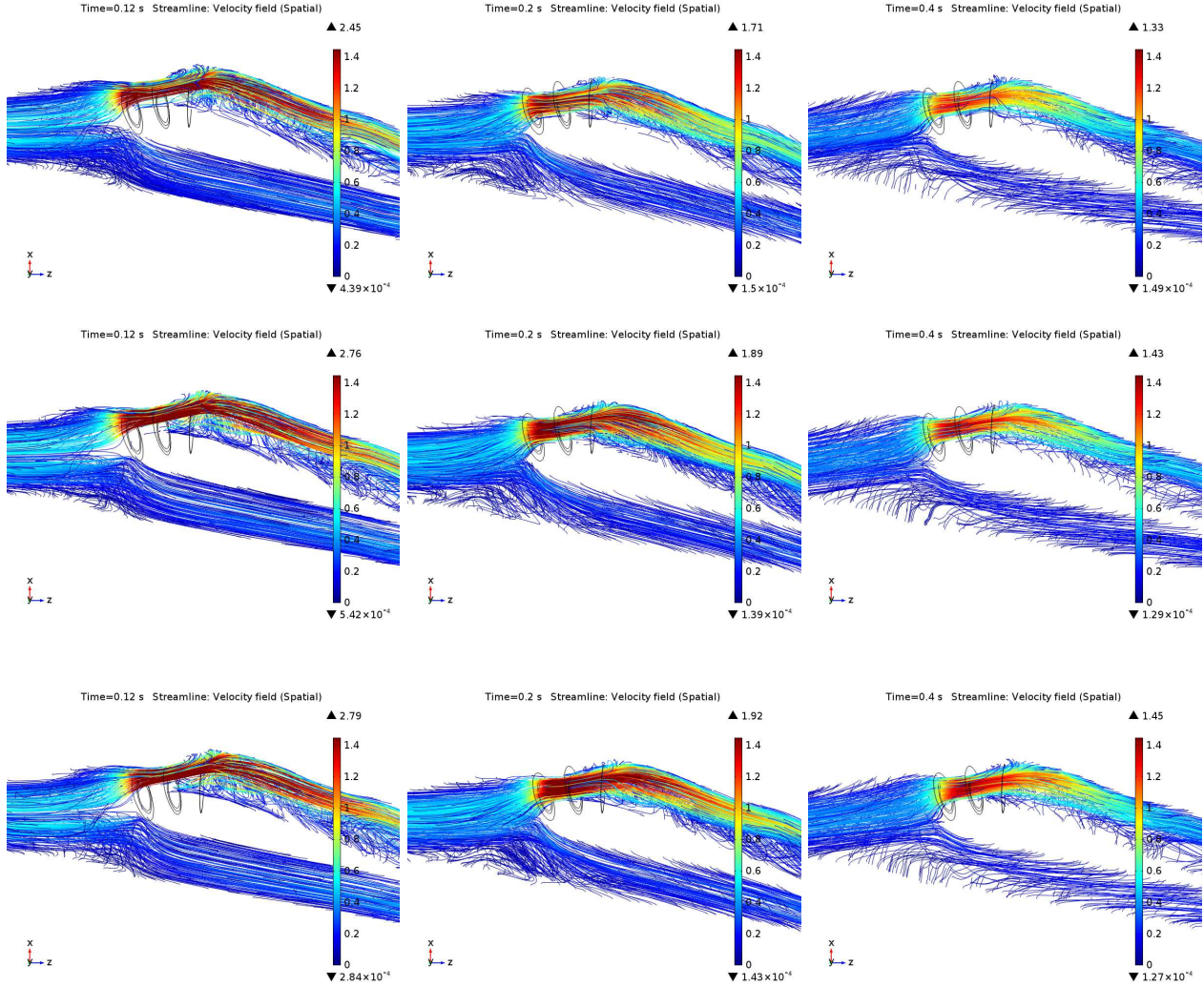


FIGURE 6. Velocity streamlines (m/s) at $t = 0.12$ s, 0.2 s, 0.4 s. First row: MR-H; second row: NL-H; third row: calcified model.

the stenotic region. The NL-H model slightly overestimates the values produced by the MR-H model. Paying attention to the position of the plaque at $t = 0$ s (black circular edges), we can see that the highest velocity values coincide with a large displacement of the unhealthy branch. As to the flow structures indicated by streamlines, one can notice that there are no significant differences between models. For the three models, one remarks that the flow is disturbed during the systolic phase (up to $t = 0.2$ s), forming recirculations downstream the stenosis. At $t = 0.4$ s, the flow tends to stabilize in this region. This is not the case in the healthy branch of the carotid, where the flow forms recirculations close to the inlet pressure's peak (see Fig. 2), remaining disturbed after that. The three models are, therefore, consistent in showing recirculation zones in the stenotic branch. Those are associated, together with other factors, with thrombus formation on the wall [31]. Besides, disturbed flow induces crucial proatherogenic pathways in endothelial cells, including endothelial inflammation and dysfunction, permeability dysfunction, thrombosis, and endothelial-to-mesenchymal transition [1].

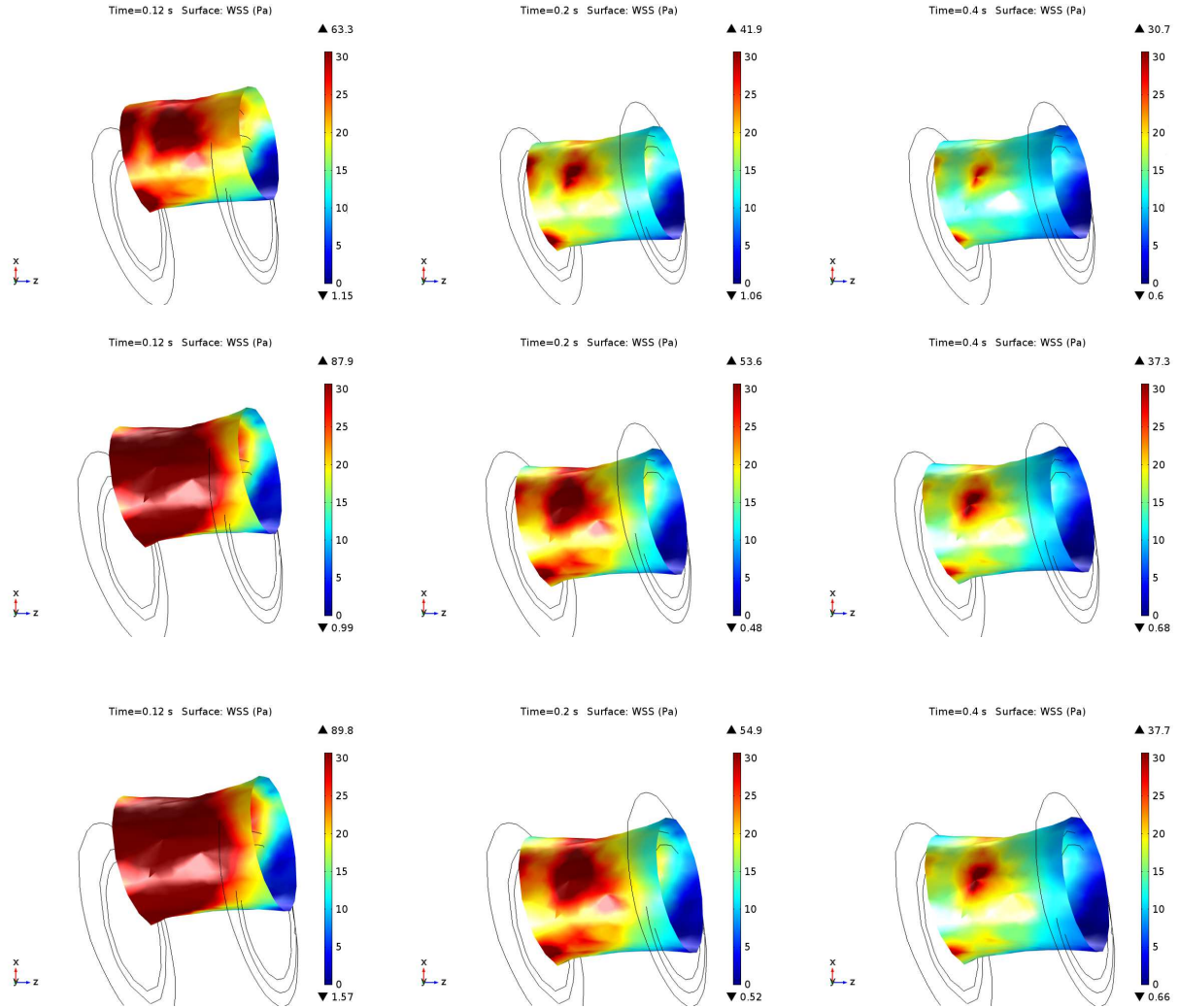


FIGURE 7. The WSS profile in the fibrous cap surface (Pa) at $t = 0.12$ s, 0.2 s, 0.4 s. First row: MR-H; second row: NL-H; third row: calcified model.

3.2. WSS distribution

Figure 7 shows the WSS distributions on the surface of the fibrous cap. Comparing the three cases, one may observe that for both NL-H and calcified models, the WSS values are higher and cover almost all the surface, at the systolic phase. The MR-H model shows substantially a big difference in the distribution of the WSS maximum values. As expected those values are concentrated in the areas adjacent to the upstream and downstream districts of the artery. In Figure 9 (left), we can see the evolution of the WSS average along one cardiac cycle. The results are consistent with what was observed in Figure 7 showing higher values for the same two models along the cardiac cycle. WSS is thought to determine the site-specific preference of atherosclerosis [10], where fatty streaks and atheromatous plaque were found to be distributed in regions of low WSS [33] such as the carotid bifurcations [27]. These results are somewhat consistent with other studies [26, 45] where authors

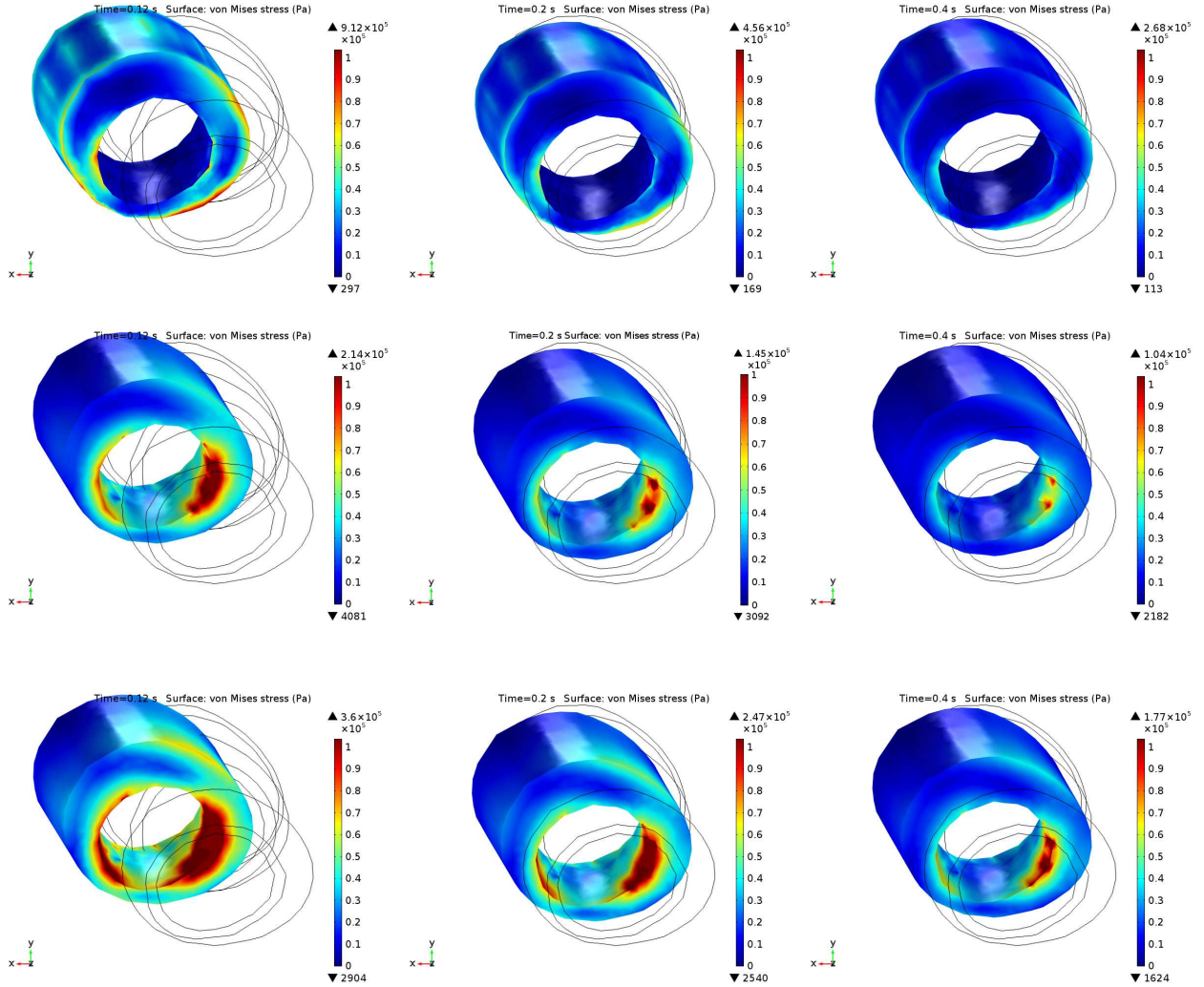


FIGURE 8. The von Mises stress distribution (Pa) at $t = 0.12\text{ s}$, 0.2 s , 0.4 s . First row: MR-H; second row: NL-H; third row: calcified model.

distinguish between a stenotic plaque with high WSS, thick fibrous cap and small lipid core, and a vulnerable plaque with low WSS, thin fibroatheromatous cap and large necrotic lipid core.

3.3. von Mises stress

Another relevant quantity that was computed, is the von Mises stress to show the sites of expected failure. The von Mises theory [44] of failure assumes that the material fails when a maximum value exceeds a failure threshold characteristic of that material. Based on the assumption that there is a correlation between the locations of maximal von Mises stress concentration and plaque rupture, Figure 8 shows high stress regions of plaque. The MR-H model is the one with the highest risk of rupture in the shoulder region of the plaque (912kPa at $t = 0.12\text{ s}$). However, for the NL-H and calcified models the maximal values are observed in the fibrous cap. Therefore, the results in Figure 9 showing the average values of this stress demonstrated the big gap between the NL-H and calcified models and the MR-H model where the values are almost negligible. One

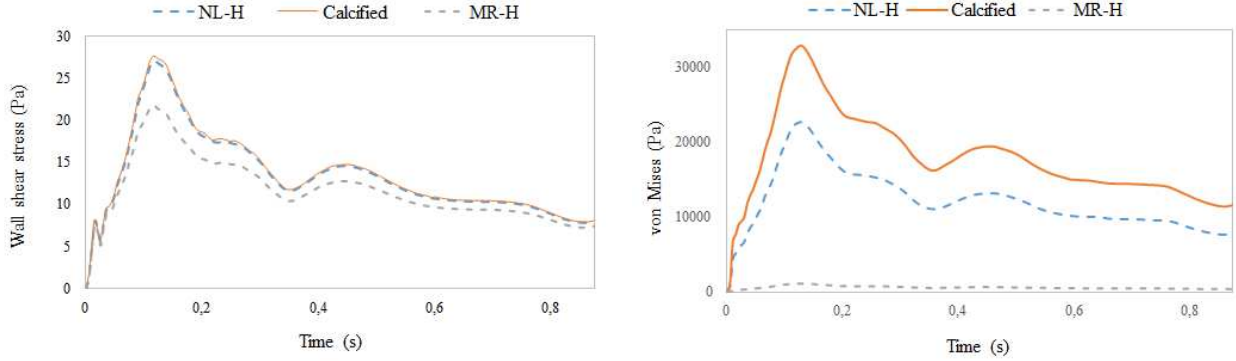


FIGURE 9. Comparison between the average values of WSS (left) and the von Mises stress (right) in the fibrous cap and the plaque, respectively.

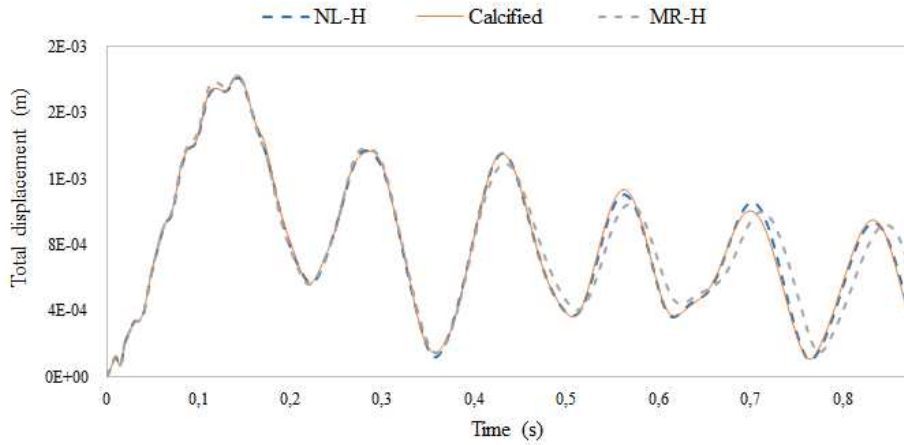


FIGURE 10. Comparison between the average values of the total displacement of the plaque.

can notice that for the two first models those average distributions curves follow the same shape of the inlet pressure waveform, while for the MR-H model these distributions tend to zero, possibly due to the elasticity of the wall and the plaque chosen for different models.

3.4. Carotid displacement

Carotid motion analysis is also considered as a potential index of plaque vulnerability [17, 43]. It can be defined as the estimation of arterial tissue displacement during one or more cardiac cycles [18]. As mentioned above, Figures 6, 7 and 8 allow us to perceive the relative motion between the plaque and the adjacent wall, as well as within the plaque itself. For that purpose, the contours surrounding the plaque region were kept in the initial position to show the displacement of the structure in the real scale (black circular edges). In the three cases, practically, there is no significant difference for the displacement in the longitudinal direction. This is consistent with the average values shown in Figure 10. In contrast, an enlargement in the radial direction is observed in the MR-H model (see Fig. 7) confirming the hypothesis that vascular calcification may directly increase arterial stiffness [29]. This is in agreement with several clinical studies demonstrating an association between arterial

stiffness and atherosclerotic burden as well as between arterial stiffness and incident cardiovascular events (see [36] and references therein).

4. CONCLUSIONS

This work presents a noninvasive approach for quantifying hemodynamic parameters and structural stress (using different material assumptions for the atheromatous plaque) at the human carotid bifurcation with stenosis. The first part consists of reconstructing whole 3D geometry based on the medical image derived from the MRI. Then a 3D FSI model incorporating fluid-structure interaction (blood-plaque and blood-wall), with different hyperelastic material assumptions, as well as non-Newtonian effects, is used to analyze the flow and structures stresses. The three models considered show disturbed flow in the atherosclerotic area, as indicated in previous findings. The WSS is, as expected, globally higher in the stenotic area, being smaller for the MR-H, which allows for some compressibility in the plaque region. Concerning the von Mises Stress, the MR-H model provides highly localized values, indicating a higher risk of rupture on the shoulder of the plaque, when compared with the other two material assumptions, which indicates higher risk of rupture on the fibrous cap. The methodology provided realistic simulations and meaningful analysis, while using relatively low computational power (see *e.g.* [3]). We believe, therefore, that this methodology may be applied to more patient-specific systematic analysis.

Acknowledgements. This work was supported by FCT – Fundação para a Ciência e Tecnologia through the CEMAT projects UIDB/04621/2020/IST-ID, UIDP/04621/2020/IST-ID and the research project PTDC/MAT-APL/7076/2020.

REFERENCES

- [1] A. Andueza, S. Kumar, J. Kim, D.-W. Kang, H.L. Mumme, J.I. Perez, N. Villa-Roel and H. Jo, Endothelial reprogramming by disturbed flow revealed by single-cell RNA and chromatin accessibility study. *Cell Rep.* **33** (2020) 108491.
- [2] Y. Bazilevs, V.M. Calo, T.E. Tezduyar and T.J.R. Hughes, Beta discontinuity capturing for advection-dominated processes with application to arterial drug delivery. *Int. J. Numer. Meth. Fluids* **54** (2007) 593–608.
- [3] L. Bennati, C. Vergara, M. Domanin, C. Malloggi, D. Bissacco, S. Trimarchi, V. Silani, G. Parati and R. Casana, A computational fluid-structure interaction study for carotids with different atherosclerotic plaques. *J. Biomech. Eng.* **143** (2021). <https://doi.org/10.1115/1.4050910>.
- [4] S. Boujena, O. Kafi and N. El Khatib, Generalized Navier–Stokes equations with non-standard conditions for blood flow in atherosclerotic artery. *Appl. Anal.* **95** (2016) 1645–1670.
- [5] A.N. Brooks and T.J.R. Hughes, Streamline upwind/Petrov-Galerkin formulations for a convection dominated flows with a particular emphasis on the incompressible Navier–Stokes equations. *Comput. Meth. Appl. Mech. Eng.* **32** (1982) 199–259.
- [6] C.M. Buffinton and D.M. Ebenstein, Effect of calcification modulus and geometry on stress in models of calcified atherosclerotic plaque. *Cardiovasc. Eng. Tech.* **5** (2014) 244–260.
- [7] Z. Chen, H. Qin, J. Liu, B. Wu, Z. Cheng, Y. Jiang, L. Liu, L. Jing, X. Leng, J. Jing and Y. Wang, Characteristics of wall shear stress and pressure of intracranial atherosclerosis analyzed by a computational fluid dynamics model: a pilot study. *Front. Neurol.* **10** (2020). doi: [10.3389/fneur.2019.01372](https://doi.org/10.3389/fneur.2019.01372).
- [8] P.G. Ciarlet, *Mathematical Elasticity*. Vol. 1 of *Three Dimensional Elasticity*. North-Holland (1988).
- [9] P. Crosetto, P. Raymond, S. Deparis, D. Kontaxakis, N. Stergiopoulos and A. Quarteroni, Fluid-structure interaction simulations of physiological blood flow in the aorta. *Comput. Fluids* **43** (2011) 46–57.
- [10] S.S. Dhawan, R.P. Avati Nanjundappa, J. R. Branch, W. Robert Taylor, A.A. Quyyumi, H. Jo, M.C. McDaniel, J. Suo, D. Giddens and H. Samady, Shear stress and plaque development. *Expert Rev. Cardiovasc. Ther.* **8** (2010) 545–556.
- [11] P. Deuffhard, A modified newton method for the solution of ill-conditioned systems of nonlinear equations with application to multiple shooting. *Numer. Math.* **22** (1974) 289–315.
- [12] J. Donea, S. Giuliani and J.P. Halleux, An arbitrary Lagrangian–Eulerian finite element method for transient dynamic fluid-structure interactions. *Comput. Methods Appl. Mech. Eng.* **33** (1982) 689–723.
- [13] N. El Khatib, *Modélisation mathématique de l’athérosclérose*. PhD thesis, Université Claude Bernard–Lyon 1, 2009.
- [14] N. El Khatib, O. Kafi, J. Tiago and A. Sequeira, Numerical simulations of a 3D fluid-structure interaction model for blood flow in an atherosclerotic artery. *Math. Biosci. Eng.* **14** (2017) 179–193.

- [15] E. Faggiano, L. Formaggia and L. Antiga, An open-source tool for patient-specific fluid-structure vessel mesh generation. Fifth International Symposium on Modelling of Physiological Flows, Chia Laguna, Italy, 2013.
- [16] A.M. Gambaruto, J. Janela, A. Moura and A. Sequeira, Sensitivity of hemodynamics in a patient specific cerebral aneurysm to vascular geometry and blood rheology. *Math. Biosci. Eng.* **8** (2011) 409–423.
- [17] A. Gastouniotti, S. Makrodimitis, S. Golemati, N.P.E. Kadoglou, C.D. Liapis and K.S. Nikita, A novel computerized tool to stratify risk in carotid atherosclerosis using kinematic features of the arterial wall. *IEEE J. Biomed. Health Inform.* **19** (2015) 1137–1145.
- [18] S. Golemati, E. Patelaki, A. Gastouniotti, I. Andreadis, C.D. Liapis and K.S. Nikita, Motion synchronisation patterns of the carotid atheromatous plaque from B-mode ultrasound. *Sci. Rep.* **10** (2020) 11221.
- [19] T. Guerra, A. Sequeira and J. Tiago, Optimal control in blood flow simulations. *Int. J. Non-linear Mech.* **64** (2014) 57–69.
- [20] G.K. Hansson and J. Nilsson, Developing a vaccine against atherosclerosis. *Nat. Rev. Cardiol.* **17** (2020), 451–452.
- [21] G. Hauke and T.J.R. Hughes, A unified approach to compressible and incompressible flows. *Comput. Meth. Appl. Mech. Eng.* **113** (1994) 389–395.
- [22] A. Hindmarsh, P. Brown, K. Grant, S. Lee, R. Serban, D. Shumaker and C. Woodward, Sundials: suite of non-linear and differential/algebraic equation solvers. *ACM Trans. Math. Softw.* **31** (2005) 363–396.
- [23] T.J.R. Hughes, W.K. Liu and T.K. Zimmermann, Arbitrary Lagrangian–Eulerian finite element formulation for incompressible viscous flows. *Comput. Method Appl. M.* **29** (1981) 329–349.
- [24] J. Janela, A. Moura and A. Sequeira, A 3D non-Newtonian fluid-structure interaction model for blood flow in arteries. *J. Comput. Appl. Math.* **234** (2010) 2783–2791.
- [25] J. Janela, A. Moura and A. Sequeira, Absorbing boundary conditions for a 3D non-Newtonian fluid-structure interaction model for blood flow in arteries. *Int. J. Eng. Sci.* **48** (2010) 1332–1349.
- [26] Y. Jiang, K. Kohara and K. Hiwada, Association between risk factors for atherosclerosis and mechanical forces in carotid artery. *Stroke* **5** (2000) 2319–2324.
- [27] D. Ku, D. Giddens, C. Zarins and S. Glagov, Pulsatile flow and atherosclerosis in the human carotid bifurcation. Positive correlation between plaque location and low oscillating shear stress. *Arterioscler. Thromb. Vasc. Biol.* **5** (1985) 293–302.
- [28] Z.Y. Li, S. Howarth, R.A. Trivedi, J.M. U-King-Im, M.J. Graves, A. Brown, L. Wang and J.H. Gillard, Stress analysis of carotid plaque rupture based on in vivo high resolution MRI. *J. Biomech.* **39** (2006) 2611–2622.
- [29] R.H. Mackey, L. Venkitachalam and K. Sutton-Tyrrell, Calcifications, arterial stiffness and atherosclerosis. *Adv. Cardiol.* **44** (2007) 234–244.
- [30] J.B. Mendieta, D. Fontanarosa, J. Wang, K.P. Paritala, T. McGahan, T. Lloyd and Z. Li, The importance of blood rheology in patient-specific computational fluid dynamics simulation of stenotic carotid arteries. *Biomech. Model Mechanobiol.* (2020). <https://doi.org/10.1007/s10237-019-01282-7>.
- [31] C. Menichini and X. Yun Xu, Mathematical modeling of thrombus formation in idealized models of aortic dissection: initial findings and potential applications. *J. Math. Biol.* **73** (2016) 1205–1226.
- [32] J. Moradicheghamahi, J. Sadeghiseraji and M. Jahangiri, Numerical solution of the Pulsatile, non-Newtonian and turbulent blood flow in a patient specific elastic carotid artery. *Int. J. Mech. Sci.* **150** (2019) 393–403.
- [33] J. Mustard, H. Rowsell, E. Murphy, H. Downie and R.J. Jones, Evolution of Atherosclerotic Plaque. University of Chicago Press, IL, USA (1963).
- [34] F. Nobile, Numerical Approximation of Fluid-Structure Interaction Problems with Application to Hemodynamics. PhD thesis, École Polytechnique Fédérale de Lausanne, 2001.
- [35] D. Oliveira, S. Aguiar Rosa, J. Tiago, R. Cruz Ferreira, A. Figueiredo Agapito and A. Sequeira, Bicuspid aortic valve aortopathies: an hemodynamics characterization in dilated aortas. *Comput. Method Biomech.* **22** (2019) 815–826.
- [36] C. Palombo and M. Kozakova, Arterial stiffness, atherosclerosis and cardiovascular risk: pathophysiologic mechanisms and emerging clinical indications. *Vasc. Pharmacol.* **77** (2016) 1–7.
- [37] PARDISO. 2018. www.pardiso-project.org
- [38] C.G. Petra, O. Schenk, M. Lubin and K. Gärtner, An augmented incomplete factorization approach for computing the Schur complement in stochastic optimization. *SIAM J. Sci. Comput.* **36** (2014) 139–162.
- [39] E. Qaja, P. Tadi and P. Theetha Kariyanna, Carotid Artery Stenosis. StatPearls, Treasure Island (FL), January (2020).
- [40] S. Ramalho, A. Moura, A. Gambaruto and A. Sequeira, Sensitivity to outflow boundary conditions and level of geometry description for a cerebral aneurysm. *Int. J. Numer. Method Biomed. Eng.* **28** (2012) 697–713.
- [41] F. Shakib, T.J.R. Hughes and Z. Johan, A new finite element formulation for computational fluid dynamics. X. The compressible Euler and Navier–Stokes equations. *Comput. Meth. Appl. Mech. Eng.* **89** (1991) 141–219.
- [42] D. Tang, C. Yang, J. Zheng, P.K. Woodard, G.A. Sicard, J.E. Safitz and C. Yuan, 3D MRI-based multicomponent FSI models for atherosclerotic plaques. *Ann. Biomed. Eng.* **32** (2004) 947–960.
- [43] J. Tat, I.N. Psaromiligkos and S.S. Daskalopoulou, Carotid atherosclerotic plaque alters the direction of longitudinal motion in the artery wall. *Ultrasound Med. Biol.* **42** (2016) 2114–2122.
- [44] A.C. Ugural and S.K. Fenster, Advanced Strength and Applied Elasticity. Prentice-Hall, Upper Saddle River, NJ (1995).
- [45] J.J. Wentzel, R. Corti, Z.A. Fayad, P. Wisdom, F. Macaluso, M.O. Winkelman, V. Fuster and J.J. Badimon, Does shear stress modulate both plaque progression and regression in the thoracic aorta? Human study using serial magnetic resonance imaging. *J. Am. Coll. Cardiol.* **45** (2005) 846–854.

- [46] K.K. Wong, P. Thavornpattanapong, S.C.P. Cheung, Z. Sun and J. Tu, Effect of calcification on the mechanical stability of plaque based on a three-dimensional carotid bifurcation model. *BMC Cardiovasc. Disord.* **12** (2012). <https://doi.org/10.1186/1471-2261-12-7>.



Please help to maintain this journal in open access!

This journal is currently published in open access under the Subscribe to Open model (S2O). We are thankful to our subscribers and supporters for making it possible to publish this journal in open access in the current year, free of charge for authors and readers.

Check with your library that it subscribes to the journal, or consider making a personal donation to the S2O programme by contacting subscribers@edpsciences.org.

More information, including a list of supporters and financial transparency reports, is available at <https://edpsciences.org/en/subscribe-to-open-s2o>.